Tuning the spin qubit property of diamagnetic Zn(II) metal– organic frameworks via Cu(II) doping

Masanori Wakizaka (ma-wakiz@photon.chitose.ac.jp)
Chitose Institute of Science and Technology https://orcid.org/0000-0002-2999-8842
Shraddha Gupta
Tohoku University
Qingyun Wan
The University of Hong Kong
Shinya Takaishi
Tohoku University
Honoka Noro
Osaka Metropolitan University
Kazunobu Sato (sato@omu.ac.jp)
Osaka Metropolitan University
Masahiro Yamashita (yamasita@agnus.chem.tohoku.ac.jp)
Tohoku University

Research Article

Keywords: Metal-organic framework, Hybrid organic-inorganic perovskite, Spin qubit, Magnetism, Cupper(II)

DOI: https://doi.org/

Tuning the spin qubit property of diamagnetic Zn(II) metal–organic frameworks via Cu(II) doping

Masanori Wakizaka,[1]* Shraddha Gupta,[2] Qingyun Wan,[3] Shinya Takaishi,[3] Honoka Noro,[4] Kazunobu Sato,[4]* and Masahiro Yamashita[2,5]*

[1] Department of Applied Chemistry and Bioscience, Faculty of Science and Technology, Chitose Institute of Science and Technology, 758-65 Bibi, Chitose 066-8655, Japan.

[2] Department of Chemistry, Graduate School of Science, Tohoku University, 6-3 Aramaki-Aza-Aoba, Aoba-Ku, Sendai 980-8578, Japan. Fax: +81-22-795-6548; Tel: +81-22-795-6544.

[3] Department of Chemistry, State Key Laboratory of Synthetic Chemistry, HKU-CAS Joint Laboratory on New Materials, The University of Hong Kong.

[4] Department of Chemistry, Graduate School of Science, Osaka Metropolitan University, 3-3-138 Sugimoto, Sumiyoshi-ku, Osaka 558-8585, Japan.

[5] School of Materials Science and Engineering, Nankai University, Tianjin 300350, P. R. China

E-mail: ma-wakiz@photon.chitose.ac.jp, sato@omu.ac.jp, yamasita@agnus.chem.tohoku.ac.jp

Key Words: Metal-organic framework, Hybrid organic-inorganic perovskite, Spin qubit, Magnetism, Cupper(II)

Abstract

With the aim of developing a general method for the synthesis of molecular spin qubits, this work demonstrates a spin-center doping method based on the use of a metal–organic framework (MOF). As the MOF host, perovskite-type $[CH_6N_3][Zn^{II}(HCOO)_3]$ doped with 5%, 2%, and 1% mol of Cu(II) ions is used. An analysis including X-ray fluorescence spectroscopy, magnetism, and the complete active space self-consistent field calculation method confirm the presence of dopant Cu(II) sites with the $S = 1/2$ system. Magnetic dynamics indicate the occurrence of a slow magnetic relaxation via the Raman process under an applied field, with a relaxation time of 3.5 ms (5% Cu), 9.2 ms (2% Cu), and 15 ms (1% Cu) at 1.8 K. Furthermore, pulse electron spin resonance spectroscopy reveals spin qubit properties with a Hahn echo decay time of 0.24 μs (2% Cu) and 0.41 μs (1% Cu) at 4 K as well as Rabi oscillation between $M_S = \pm 1/2$ spin sublevels. These relaxation-extending effects stem from the weakening of the spin–spin interactions between the Cu(II) sites and can be tuned by adjusting the dopant concentration. This work demonstrates a new application of MOFs as quantum materials having fine-tuning ability for spin qubits.

Introduction

Spin qubits are promising units that can work at higher temperatures than superconducting qubits, which generally operate at the milliKelvin scale.[1–5] Examples of materials exhibiting spin qubit properties, which are based on the superposition of quantum spin states, particularly two spin sublevels of M_S = ±1/2 in the S = 1/2 system because of their relatively stable spin coherence, are $[V^{IV}O(\text{-}C_3S_5)_2]^{2-}$,[6] $[V^{IV}O(\text{dipivaloylmethanato})_2]$,[7] low-spin $[M(CN)_6]^{3-}$ (M = Fe^{III}, Ru^{III}, Os^{III}),[8] low-spin $[Ni^{III}(mnt)_2]^-$ (mnt = maleonitriledithiolato),[9,10] $[Cu^{II}(mnt)_2]$,[11] and $[Cu^{II}(\text{phthalocyaninato})]$.[12] Aside from such molecular spin qubits, the diamond nitrogen-vacancy center has been reported as a solid-state qubit with stable spin coherence,[13–15] in which the very rigid framework is considered to suppress decoherence due to spin-lattice relaxation and the sparse vacancy centers contribute to weaken the spin–spin interactions by isolation.

For the construction of spin qubits, metal–organic frameworks (MOFs) are desirable materials because their structures and properties can be tuned by varying the metal ions and organic linkers.[16–19] Three methods can be used to synthesize spin qubits using MOFs, i.e., the molecular building block method (Fig. 1a),[20] the diamagnetic-center doping method (Fig. 1b),[21] and the spin-center doping method (Fig. 1c),[22–29] among which the spin center doping method is especially attractive because of its simple procedure involving the self-assembly of solvated metal ions and linkers and wide application. Šimėnas et al. reported the spin qubit properties of doped MOFs with perovskite

compositions,[30–32] i.e., high-spin Mn^{II}-doped $[CH_3(NH_2)_2][Zn^{II}(HCOO)_3]$ with a spin–spin relaxation time (T_2) of ~0.5 μs at 40 K (note that T_2 is also called phase memory time; T_m)[25] and high-spin Co^{II}-doped $[(CH_3)_2NH_2][Zn^{II}(HCOO)_3]$ with T_2 = ~0.045 (X-band) and ~0.07 (Q-band) μs at 5 K.[29] They also described the occurrence of tunnel coherence related to phase transition due to methyl group rotation in the cation moieties.[27] However, the concentration dependency of the doping sites for spin qubit properties is still unknown, as are the magnetic properties of such doped spin qubit MOFs. In addition, although some studies have reported slow magnetic relaxation in Cu(II) complexes,[33–35] there is no report on both slow magnetic relaxation and spin coherence properties.

Previously, a doped MOF, i.e., $[CH_6N_3][Co^{II}_xZn^{II}_{1-x}(HCOO)_3]$ ($[CH_6N_3]^+$ = guanidium; x = 0.01, 0.005, 0.002), was reported to exhibit single-ion magnetism with a positive D term of zero-field-splitting in a S = 3/2 system.[36] Since this guanidium-type MOF is more simple than that containing $[CH_3(NH_2)_2]^+$ because it lacks a phase transition derived from cations,[37] it seems a suitable candidate to investigate the slow magnetic relaxation and spin coherence phenomena. Herein, the systematic doping of Cu(II) into diamagnetic $[CH_6N_3][Zn^{II}(HCOO)_3]$ (Zn-MOF, Figure 2a) is reported, and the concentration dependency of magnetic dynamism and spin qubit properties in the S = 1/2 system is discussed.

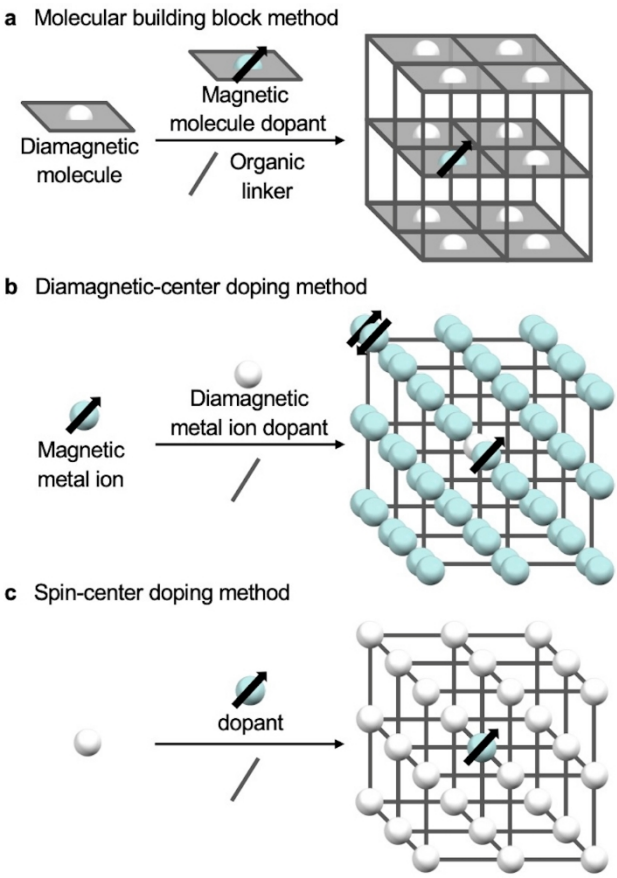

Figure 1. Schematic of the general methods to prepare MOF-based spin qubits, e.g., $[V^{IV}_{x}Ti^{IV}_{1-x}O(TCPP\text{-}Zn_2\text{-}bpy)]$ (TCPP = tetracarboxylphenylporphyrinate; bpy = 4,4′-bipyridyl),[20] $[Zn_{0.03}Cu_{2.97}(tricarboxylate)_2]$,[21] and $[CH_3(NH_2)_2][Mn^{II}_{x}Zn^{II}_{1-x}(HCOO)_3]$:[25] (a) molecular building block method, (b) diamagnetic-center doping method, and (c) spin-doping method.

Results and Discussion

The crystal structure of the Cu(II)-doped Zn-MOFs, i.e., Cu/Zn-MOF(5%), Cu/Zn-MOF(2%), and Cu/Zn-MOF(1%), was determined via powder X-ray diffraction (PXRD), which confirmed that they are isomorphous with pristine Zn-MOF (Fig. 2a). The presence of the doping Cu element was qualitatively confirmed by X-ray fluorescence (XRF) spectroscopy (Fig. 2b and S1). The Cu-Kα and Zn-Kα peaks were detected at 8.04 and 8.63 keV, respectively, and were accompanied by those of Cu-Kβ (8.90 keV) and Zn-Kβ (9.57 keV). Using the fundamental parameter method, the doped amount of Cu was estimated to be 5.2%, 2.2%, and 1.0% mol relative to Zn, which is consistent with each loading amount (5%, 2%, and 1%, respectively). Figure 3 shows the magnetization–field (M–H) curves of the Cu/Zn-MOFs. Almost saturation at a higher field region at 1.8 K can be observed (Fig. 3a), and the saturation magnetization is consistent with the loading amount. These curves are different from that of a pristine Cu-MOF having canted-spin antiferromagnetism with hysteresis (Fig. S2),[37] suggesting that the Cu/Zn-MOFs are sufficient diluted to prevent three-dimensional magnetism. In contrast, Zn-MOF does not show any magnetization, which indicates that the magnetism is not due to impurities but to the doping Cu(II) sites. Furthermore, the complete active space self-consistent field (CASSCF) calculation using the program Orca afforded anisotropic g-factors in the $S = 1/2$ system, i.e., $g_x = 2.09$, $g_y = 2.12$, and $g_z = 2.52$ (Table S1),[38] which is almost consistent with those of electron spin resonance (ESR), i.e., $g_x = 2.065$, $g_y = 2.120$, and $g_z = 2.435$ (*vide infra*). The temperature dependency of the M–H

curves shown in Figs. 3b–3d matched well with those simulated using the PHI program,[39] supporting that the magnetism stems from the doping Cu(II) sites.

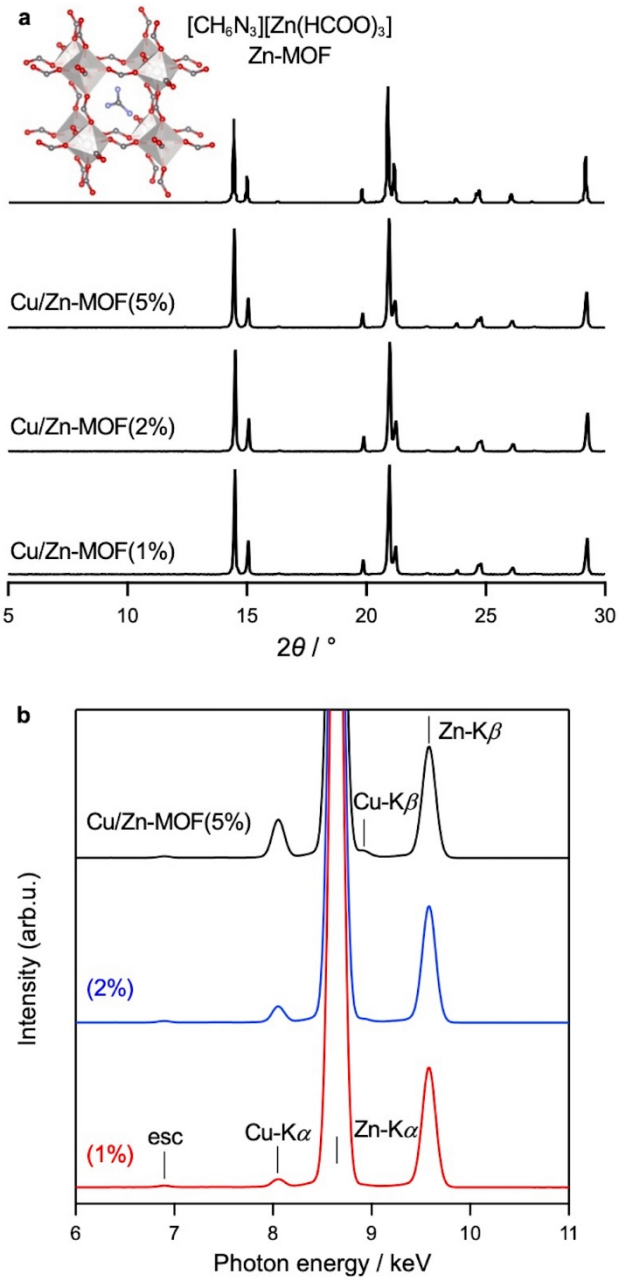

Figure 2. (a) PXRD patterns and (b) XRF spectra of Cu/Zn-MOF(5%), Cu/Zn-MOF(2%), and Cu/Zn-MOF(1%) and the crystal structure and PXRD pattern of $[CH_6N_3][Zn(HCOO)_3]$ (Zn-MOF).[37] The escape (esc) peak stems from Cu-Kα.

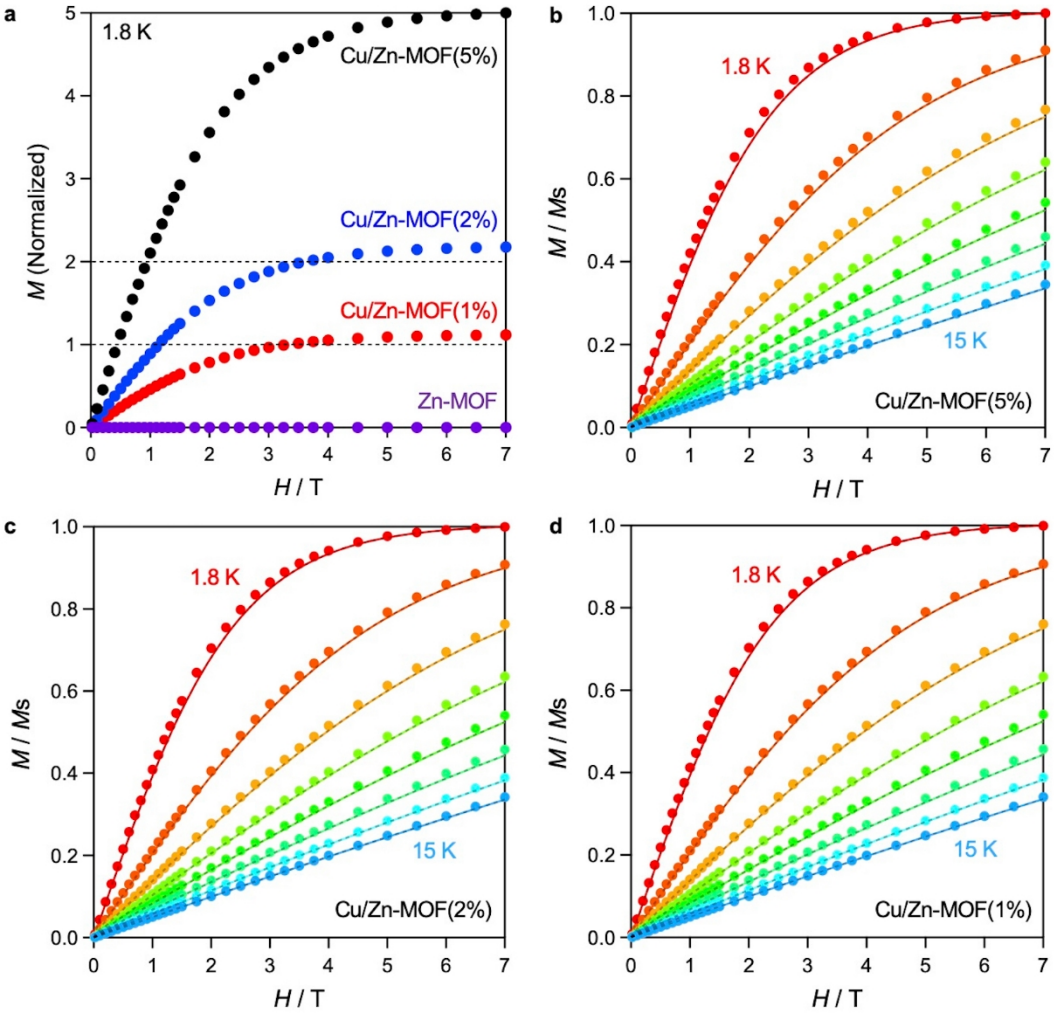

Figure 3. Magnetization–field (*M*–*H*) curves normalized by the saturation *M* (M_S) at 1.8 K of (a, b) Cu/Zn-MOF(5%), (c) Cu/Zn-MOF(2%), and (d) Cu/Zn-MOF(1%). The temperature dependency was measured at 1.8, 3.6, 5.4, 7.2, 9.0, 11, 13, and 15 K. The solid colored curves and the dotted gray curves (they are overlapping) represent the normalized simulation curves using the values obtained from CASSCF, i.e., g_x = 2.09, g_y = 2.12, g_z = 2.52, and ESR, i.e., g_x = 2.065, g_y = 2.120, and g_z = 2.435, respectively.

Although the Cu/Zn-MOFs did not show any signals on alternating current (AC) susceptibility measurements in the absence of an applied field, such signals were observed under a magnetic field (Fig. S3 and Table S2). Figure 4 shows the imaginary part of the AC susceptibility (χ'') of the Cu/Zn-doped MOFs under an applied field of 0.4 T. The real parts (χ') and the Cole–Cole plots are shown in Fig. S4. The χ'' values obtained at various temperatures were fitted using the Debye relaxation equation (equation 1):[40]

$$\chi'' = (\chi_T - \chi_S)\frac{(2\pi f\tau)^{1-\alpha}\cos(\pi\alpha/2)}{1 + 2(2\pi f\tau)^{1-\alpha}\sin(\pi\alpha/2) + (2\pi f\tau)^{2-2\alpha}} \qquad (1)$$

Here, χ_T, χ_S, f, τ, and α refer to the isothermal susceptibility, adiabatic susceptibility, AC frequency, relaxation time, and dispersion coefficient, respectively. The fitting parameters are summarized in Tables S3–S5. The peak of χ'' shows a delay of spin reversal between the quantum states of $M_S = \pm 1/2$ and the relaxation time (τ) obtained by the Debye equation. The log-scale plots of τ and temperature were fitted using a combination of the direct process and the Raman process (Fig. 4d, equations 2–4):[7]

$$\tau_{Direct} = AT^{-1} \qquad (2)$$

$$\tau_{Raman} = CT^{-m} \qquad (3)$$

$$\tau^{-1} = \tau_{Direct}^{-1} + \tau_{Raman}^{-1} \qquad (4)$$

Here, A and C are the coefficients of the direct and Raman processes, respectively, and m is the index of the Raman process. This spin-lattice relaxation is similar with that previously reported for $[V^{IV}O(\text{dipivaloylmethanato})_2]$ in the $S = 1/2$ system.[7] As a general trend, dilution slows down the relaxation, i.e., τ (Cu/Zn-MOF(5%)) < τ (Cu/Zn-MOF(2%)) < τ

(Cu/Zn-MOF(1%)), which can be explained by the weakening of the spin–spin interactions between Cu(II) centers. Particularly, Cu/Zn-MOF(1%) shows a τ of 15 ms at 1.8 K. The temperature dependency of these MOFs indicates the occurrence of a Raman process with $m = 4.4–4.7$ at a higher temperature (Table S6). Meanwhile, below ~2 K, the plots slightly deviate in the upper side from the theoretical curves, which suggests a slower relaxation induced by the phonon-bottleneck effect.

Figure 5 shows the results of X-band pulse-ESR spectroscopy measurements. Electron-spin relaxation was measured at the static magnetic field (328 mT) corresponding to the peak top of the Hahn-echo detected ESR spectrum (Fig. 5a). Spin-lattice (T_1) and T_2 relaxation times were determined by the inversion recovery method and Hahn-echo decay measurement, respectively. Both relaxation times were obtained by fitting using the following (stretched-)exponential equations (equations 5 and 6):[20]

$$I = I_0 + k\exp\left[-\left(\frac{\tau_p}{T_1}\right)^{\beta}\right] \qquad (5)$$

$$I = I_0\exp\left[-\left(\frac{2\tau_p}{T_2}\right)\right] \qquad (6)$$

Here, I, I_0, k, τ_p, and τ refer to the echo intensity, initial echo intensity, pulse separation between the initial inversion p-pulse and the two-pulse sequence for the Hahn-echo detection, pulse separation between p/2-pulse and p-pulse in the two-pulse sequence, and stretch factor, respectively. The fitting parameters are summarized in Table S7–S10. The log-scale T_1 plots are curved (Fig. 5b), suggesting the occurrence of multicomponent spin-lattice relaxation. This T_1

multicomponent relaxation, which was determined using □, is consistent with the results of the AC susceptibility measurements showing the occurrence of direct and Raman processes (Fig. 4d). In contrast, the log-scale T_2 plots lie on a straight line, suggesting a single spin–spin relaxation (Fig. 5c). T_1 and T_2 are at the microsecond and submicrosecond scales, respectively, and were measured below ~25 K. Cu/Zn-MOF(1%) shows longer T_1 and T_2 than Cu/Zn-MOF(2%) (Fig. 5d and 5e), which can be attributed to the weakening of spin–spin interactions in Cu/Zn-MOF(1%). This relaxation-extending effect is consistent with the results of the AC magnetic susceptibility measurements (Fig. 4). The longest T_1 and T_2 values of 13 ms and 0.41 □s, respectively, were obtained for Cu/Zn-MOF(1%) at 4 K. The T_1 and T_2 values of Cu/Zn-MOF(5%) could not be measured because the corresponding processes were too fast. Furthermore, Rabi oscillation was confirmed under different microwave powers using Cu/Zn-MOF(1%) at 10 K (Fig. 5f), indicating superposition of M_S = ±1/2 spin sublevels.as spin qubits.

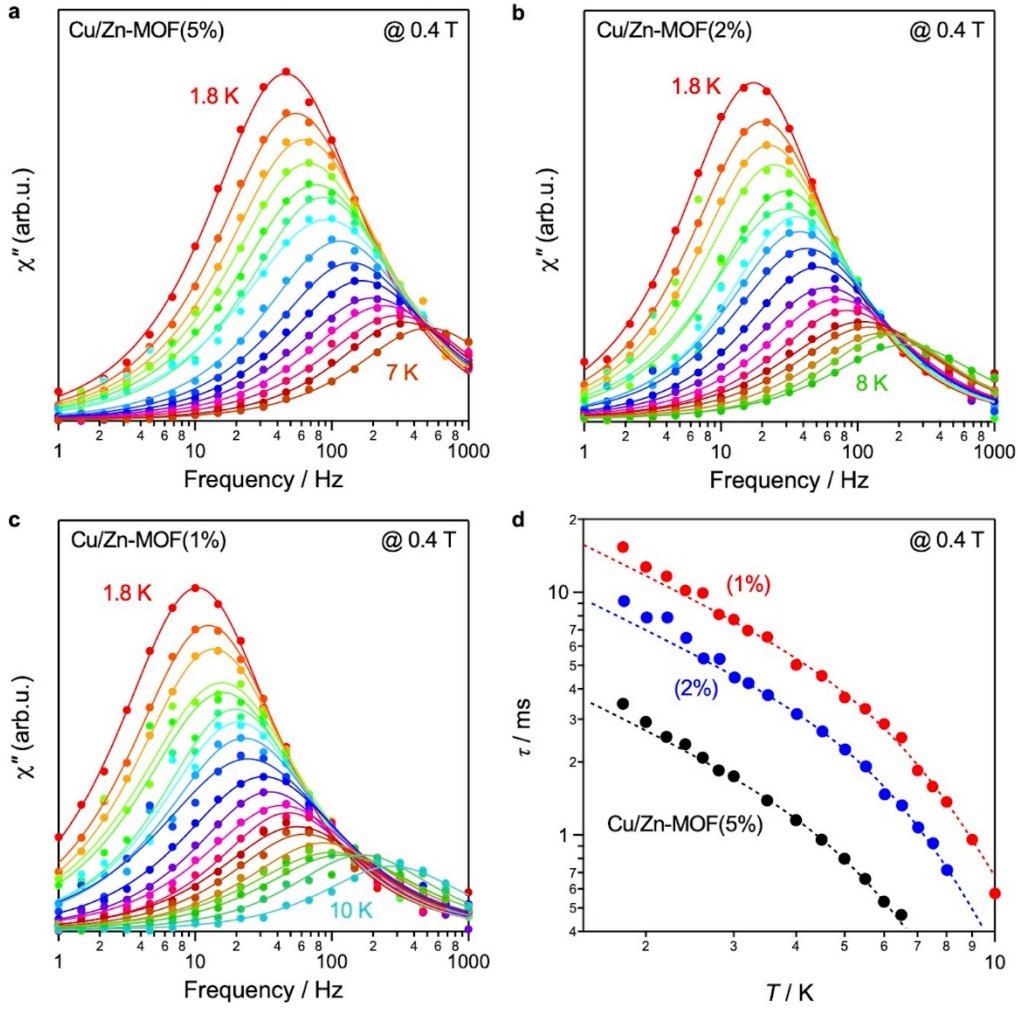

Figure 4. Imaginary part of the AC susceptibility (χ″) of (a) Cu/Zn-MOF(5%), (b) Cu/Zn-MOF(2%), and (c) Cu/Zn-MOF(1%) measured at 1.8–7.0, 1.8–8.0, and 1.8–10 K over a range of 1–1000 Hz under a static magnetic field of 0.4 T, respectively. Each line is a Debye-relaxation-fitting curve. (d) Log-scale plots of magnetic relaxation time (τ) versus temperature (*T*) for Cu/Zn-MOF(5%), Cu/Zn-MOF(2%), and Cu/Zn-MOF(1%) measured under a static magnetic field of 0.4 T. The dotted lines represent the fitting curves obtained using the direct and Raman processes.

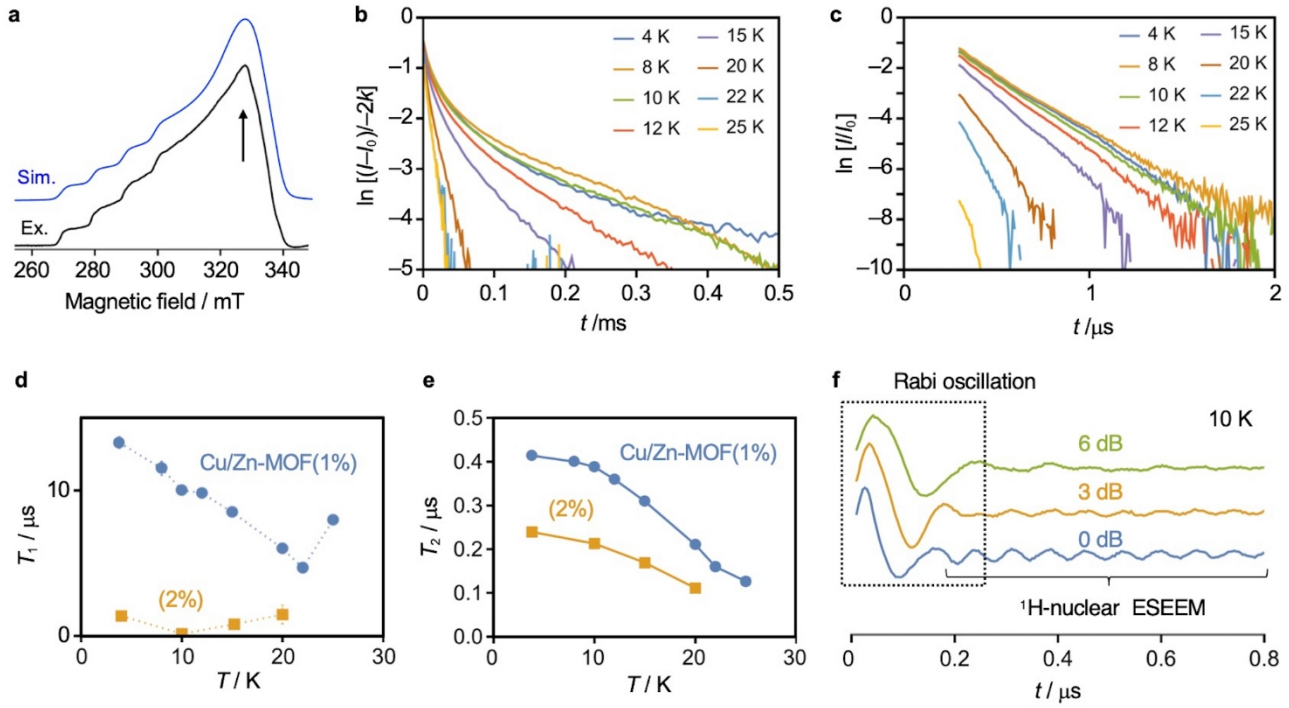

Figure 5. X-band pulse ESR measurements. (a) Hahn-echo-detected ESR spectrum of Cu/Zn-MOF(1%) at 3.8 K under microwave irradiation of 9.689126 GHz, together with that of a simulation applied g_x = 2.065(20), g_y = 2.120(60), g_z = 2.435(20), $^{Cu}A_x = {}^{Cu}A_y$ = 60 MHz, $^{Cu}A_z$ = 330 MHz, and lwpp = Gaussian (0.6 mT) + Lorentzian (0.6 mT) using EasySpin.[41] (b) Inversion recovery time (T_1) and (c) Hahn echo decay time (T_2) of Cu/Zn-MOF(1%) at 4, 8, 10, 12, 15, 20, 22, and 25 K under a magnetic field of 328 mT. Temperature dependency of (d) T_1 and (e) T_2 of Cu/Zn-MOF(1%) and Cu/Zn-MOF(2%). (f) Rabi oscillation of Cu/Zn-MOF(1%) at 10 K for different microwave powers (0, 3, and 6 dB). The fine oscillation at a later time region is due to ^{1}H electron spin echo envelope modulation (ESEEM).

Conclusions

This work demonstrated the tuning of slow magnetic relaxation and spin qubit properties in Cu-doped Zn-MOFs. It also revealed for the first time the occurrence of both magnetic dynamism and spin coherence on Cu(II) centers in the $S = 1/2$ system. The relaxation times for magnetism and spin decoherence can be tuned through the strength of spin–spin interactions by modifying the doping amount. This spin-doping method, which involves the self-assembly of Cu(II) and Zn(II) solvated ions and organic components, offers a general route for the synthesis of doped MOFs and provides a new platform for the application of MOFs as quantum materials having fine-tuning ability.

Methods

Materials. $Zn^{II}(NO_3)_2{\cdot}6H_2O$, $Cu^{II}(NO_3)_2{\cdot}3H_2O$, formic acid (HCOOH), methanol (MeOH), and *N*,*N*-dimethylformamide (DMF) were purchased from Fujifilm Wako Pure Chemical Corp. Guanidinium carbonate ($[CH_6N_3]_2CO_3$) was purchased from Sigma-Aldrich.

Synthesis of $[CH_6N_3][Zn^{II}(HCOO)_3]$ (Zn-MOF). The synthetic protocol was same as previously as follows.[36] Formic acid (811 μL, 21.5 mmol) was added into a suspension of $[CH_6N_3]CO_3$ (1.55 g, 8.60 mmol) in MeOH (20 mL), afforded a colorless solution. A solution of $Zn^{II}(NO_3)_2{\cdot}6H_2O$ (1.28 g, 4.30 mmol) in MeOH (20 mL) was dolloped into the solution with stirring at room temperature, immediately generated a precipitate. A white precipitate was collected by filtration, washed with DMF (3 × 5 mL) and MeOH (3 × 5 mL), and dried in

vacuo to afford Zn-MOF in ~100% yield.

Synthesis of $[CH_6N_3][Cu^{II}(HCOO)_3]$ (Cu-MOF). The reported synthetic protocol was modified as follows.[37] Formic acid (811 μL, 21.5 mmol) was added into a suspension of $[CH_6N_3]CO_3$ (1.55 g, 8.60 mmol) in MeOH (20 mL), afforded a colorless solution. A solution of $Cu^{II}(NO_3)_2 \cdot 3H_2O$ (1.04 g, 4.30 mmol) in MeOH (20 mL) was dolloped into the solution with stirring at room temperature, immediately generated a precipitate. A white precipitate was collected by filtration, washed with DMF (3 × 5 mL) and MeOH (3 × 5 mL), and dried in vacuo to afford Cu-MOF in ~100% yield. Elemental analysis calcd (%) for $C_4H_9N_3O_6Cu$ ($[CH_6N_3][Cu(HCOO)_3]$): C 18.57, H 3.51, N 16.24; found: C 18.72, H 3.54, N 16.32.

Synthesis of $[CH_6N_3][Cu^{II}_xZn^{II}_{1-x}(HCOO)_3]$ (Cu/Zn-MOF). The Cu(II) doped Zn-MOFs were synthesized by the same protocol above except for using $Cu^{II}(NO_3)_2 \cdot 3H_2O$ together with $Zn^{II}(NO_3)_2 \cdot 6H_2O$ (Cu: 10.5 mg, 0.0434 mmol; Zn: 1.28 g, 4.29 mmol (x = 1 %); Cu: 20.8 mg, 0.0861 mmol; Zn: 1.27 g, 4.28 mmol (x = 2 %); Cu: 51.9 mg, 0.215 mmol; Zn: 1.27 g, 4.26 mmol (x = 5 %), respectively in ~100% yields. Elemental analysis calcd (%) for $C_4H_9N_3O_6Cu_xZn_{1-x}$ ($[CH_6N_3][Cu_xZn_{1-x}(HCOO)_3]$): C 18.44, H 3.48, N 16.13; found: C 18.63, H 3.59, N 16.24 (1%); C 18.69, H 3.61, N 16.22 (2%); C 18.72, H 3.60, N 16.13 (5%).

Measurements. The elemental analysis was performed by using J-Science Lab Co. Ltd. JM11 at the Research and Analytical Center for Giant Molecules (Tohoku Univ.). XRF spectroscopy was performed by using a Rigaku NEX-DE

under an atmosphere of air. PXRD measurements were carried out with Cu-K□ radiation using a Rigaku Ultima IV diffractometer at room temperature. Magnetic measurements were performed using a magnetic property measurement system (MPMS-XL, Quantum Design) in direct current and alternating current modes. The sample was filled into a gelatin capsule (Matsuya) which was fixed in a plastic straw.

Pulse-ESR. Pulse-ESR spectra were recorded on a Bruker ESP 380 at X-band with a flexline dielectric resonator (Bruker ER 4118X-M-5) and an Oxford Instruments CF935 continuous flow helium cryostat. The customized spectrometer is fully controlled by Specman4EPR software.[42] Hahn-echo detected field-swept ESR spectra were recorded by the Hahn-echo pulse sequence (p/2–t–p–t–echo) with fixed pulse separation t = 200 ns, $t_{p/2}$ = 100 ns, and t_p = 200 ns. T_2 was measured by the Hahn-echo pulse sequence upon increasing the pulse separation t = 300 ns, $t_{p/2}$ = 50 ns, and t_p = 100 ns. T_1 was measured by the standard inversion recovery sequence (p–t_d–p/2–t–p–t–echo) with $t_{p/2}$ = 50 ns. Rabi-oscillations were measured with a nutation pulse (t_p) of variable length followed by a Hahn-echo sequence (t_p–t_d–p–t_d –echo) with t_d = 400 ns. The pulse length of the detection sequence was adjusted depending on the attenuation level.

Quantum chemical calculation. CASSCF and N-electron valence perturbation theory (NEVPT2) calculations were performed using the def2-TZVP with the AutoAux RIJCOSX basis sets on the program Orca.[38] The atomic coordinates were used from crystal structure of $[CH_6N_3][Cu^{II}(HCOO)_3]$ (Table

S1).[37] The active space was applied nine electrons and five 3d orbitals (CAS(9e,5o)) with 5 doublet states on the Cu(II) center.

Acknowledgements

This work was supported by the JSPS KAKENHI Grants (JP19H05631, JP21H01756, and JP23H01925), the TOKUYAMA Science Foundation, the Tokyo Ohka Foundation for The Promotion of Science and Technology (23108), the Nippon Sheet Glass Foundation for Materials Science and Engineering Grants, and the National Natural Science Foundation of China (NSFC, 22150710513). M.Y. thanks the 111 project (B18030) from China.

Supporting information. The Supporting Information is available free of charge on the website. XRF, *M*–*H* loop, CASSCF, AC susceptibility, AC susceptibility and magnetic relaxation fitting parameters, pulse-ESR fitting parameters (PDF).

Abbreviations. Metal–organic framework; MOF, Tetracarboxylphenylporphyrinate; TCPP, powder X-ray diffraction; PXRD, X-ray fluorescence; XRF, Magnetization–field; *M*–*H*, Complete active space self-consistent field; CASSCF, Electron spin resonance; ESR, Alternating current; AC.

Notes. The authors declare no competing financial interest.

References

(1) Moreno-Pineda, E.; Godfrin, C.; Balestro, F.; Wernsdorfer, W.; Ruben, M. Molecular spin qudits for quantum algorithms, *Chem. Soc. Rev.* **2018**, *47*, 501–513.

(2) Atzori, M.; Sessoli, R. The second quantum revolution: role and challenges of molecular chemistry, *J. Am. Chem. Soc.* **2019**, *141*, 11339–11352.

(3) Wasielewski, M. R.; Forbes, M. D. E.; Frank, N. L.; Kowalski, K.; Scholes, G. D.; Yuen-Zhou, J.; Baldo, M. A.; Freedman, D. E.; Goldsmith, R. H.; Goodson III, T.; Kirk, M. L.; McCusker, J. K.; Ogilvie, J. P.; Shultz, D. A.; Stoll, S; Whaley, K. B. Exploiting chemistry and molecular systems for quantum information science, *Nat. Rev. Chem*. **2020**, *4*, 490–504.

(4) Arute, F. et al. Quantum supremacy using a programmable superconducting processor, *Nature* **2019**, *574*, 505–511.

(5) Cao, S. et al. Quantum supremacy using a programmable superconducting processor, *Nature* **2023**, DOI: 10.1038/s41586-023-06195-1.

(6) Yu, C.-J.; Graham, M. J.; Zadrozny, J. M.; Niklas, J.; Krzyaniak, M. D.; Wasielewski, M. R.; Poluektov, O. G.; Freedman, D. E. Long coherence times in nuclear spin-free vanadyl qubits, *J. Am. Chem. Soc*. **2016**, *138*, 14678–14685.

(7) Tesi, L.; Lucaccini, E.; Cimatti, I.; Perfetti, M.; Mannini, M.; Atzori, M.; Morra, E.; Chiesa, M.; Caneschi, A.; Sorace, L.; Sessoli, R. Quantum coherence in a processable vanadyl complex: new tools for the search of molecular spin qubits, *Chem. Sci.* **2016**, *7*, 2074–2083.

(8) Graham, M. J.; Zadrozny, J. M.; Shiddiq, M.; Anderson, J. S.; Fataftah, M. S.; Hill, S.; Freedman, D. E. Influence of electronic spin and spin−orbit coupling

on decoherence in mononuclear transition metal complexes, *J. Am. Chem. Soc*. **2014**, *136*, 7623–7626.

(9) Bader, K.; Schlindwein, S. H.; Gudat, D.; Slageren, J. v. Molecular qubits based on potentially nuclear-spin-free nickel ions, *Phys. Chem. Chem. Phys.* **2017**, *19*, 2525–2529.

(10) Toshima, K.; Sato, T.; Horii, Y.; Sato, K.; Sugisaki, K.; Breedlove, B. K.; Takaishi, S.; Li, Z.-Y.; Yamashita, M. Slow magnetic relaxation of Ni(III) complexes toward molecular spin qubits, *Eur. J. Inorg. Chem.* **2023**, *2023*, e202300125.

(11) Bader, K.; Dengler, D.; Lenz, S.; Endeward, B.; Jiang, S.-D.; Neugebauer, P.; Slageren, J. v. Room temperature quantum coherence in a potential molecular qubit, *Nat. Commun*. **2014**, *5*, 5304.

(12) Warner, M.; Din, S.; Tupitsyn, I. S.; Morley, G. W.; Stoneham, A. M.; Gardener, J. A.; Wu, Z.;. Fisher, A. J.; Heutz, S.; Kay, C. W. M.; Aeppli, G. Potential for spin-based information processing in a thin-film molecular semiconductor, Nature 2013, 503, 504–508.

(13) Togan, E.; Chu, Y.; Trifonov, A. S.; Jiang, L.; Maze, J.; Childress, L.; Dutt, M. V. G.; Sørensen, A. S.; Hemmer, P. R.; Zibrov, A. S.; Lukin, M. D. Quantum entanglement between an optical photon and a solid-state spin qubit, *Nature* **2010**, *466*, 730–734.

(14) Robledo, L.; Childress, L.; Bernien, H.; Hensen, B.; Alkemade, P. F. A.; Hanson, R. High-fidelity projective read-out of a solid-state spin quantum register, *Nature* **2011**, *477*, 574–578.

(15) Maurer, P. C.; Kucsko, G.; Latta, C.; Jiang, L.; Yao, N. Y.; Bennett, S. D.; Pastawski, F.; Hunger, D.; Chisholm, N.; Markham, M.; Twitchen, D. J.; Cirac, J. I.; Lukin, M. D. Room-temperature quantum bit memory exceeding one second, *Science* **2012**, *336*, 1283–1286.

(16) Yaghi, O. M.; O'Keeffe, M.; Ockwig, N. W.; Chae, H. K.; Eddaoudi, M.; Kim, J. Reticular synthesis and the design of new materials, *Nature* **2003**, *423*, 705–714.

(17) Kitagawa, S.; Kitaura, R.; Noro, S. Functional porous coordination polymers, *Angew. Chem. Int. Ed*. **2004**, *43*, 2334–2375.

(18) Furukawa, H.; Cordova, K. E.; O'Keeffe, M.; Yaghi, O. M. The chemistry and applications of metal-organic frameworks, *Science* **2013**, *341*, 1230444.

(19) Graham, M. J.; Zadrozny, J. M.; Fataftah, M. S.; Freedman, D. E. Forging Solid-State Qubit Design Principles in a Molecular Furnace, *Chem. Mater.* **2017**. *29*, 1885–1897.

(20) Yamabayashi, T.; Atzori, M.; Tesi, L.; Cosquer, G.; Santanni, F.; Boulon, M.-E.; Morra, E.; Benci, S.; Torre, R.; Chiesa, M.; Sorace, L.; Sessoli, R.; Yamashita, M. Scaling up electronic spin qubits into a three-dimensional metal–organic framework, *J. Am. Chem. Soc*. **2018**, *140*, 12090–12101.

(21) Šimeňas, M.; Jee, B.; Hartmann, M.; Banys, J.; Pöppl, A. Adsorption and desorption of HD on the metal–organic framework $Cu_{2.97}Zn_{0.03}(Btc)_2$ studied by three-pulse ESEEM spectroscopy, *J. Phys. Chem. C* **2015**, *119*, 28530–28535.

(22) Šimeňas, M.; Ciupa, A.; Maçzka, M.; Pöppl, A.; Banys, J. EPR study of structural phase transition in manganese-doped $[(CH_3)_2NH_2][Zn(HCOO)_3]$ metal–organic framework, J. *Phys. Chem. C* **2015**, *119*, 24522–24528.

(23) Šimėnas, M.; Ciupa, A.; Mączka, M.; Völkel, G.; Pöppl, A.; Banys, J. EPR of structural phase transition in manganese- and copper–doped formate framework of $[NH_3(CH_2)_4NH_3][Zn(HCOO)_3]_2$, *J. Phys. Chem. C* **2016**, *120*, 19751–19758.

(24) Šimėnas, M.; Macalik, L.; Aidas, K.; Kalendra, V.; Klose, D.; Jeschke, G.; Mączka, M.; Völkel, G.; Banys, J.; Pöppl, A. Pulse EPR and ENDOR study of manganese doped $[(CH_3)_2NH_2][Zn(HCOO)_3]$ hybrid perovskite framework, *J. Phys. Chem. C* **2017**, *121*, 27225–27232.

(25) Šimėnas, M.; Balčiūnas, S.; Trzebiatowska, M.; Ptak, M.; Mączka, M.; Völkel, G.; Pöppl, A.; Banys, J. Electron paramagnetic resonance and electric characterization of a $[CH_3NH_2NH_2][Zn(HCOO)_3]$ perovskite metal formate framework, *J. Mater. Chem. C*, **2017**, *5*, 4526–4536.

(26) Šimėnas, M.; Ciupa, A.; Usevičius, G.; Aidas, K.; Klose, D.; Jeschke, G. Mączka, M.; Völkel, G. Pöppl, A.; Banys, J. Electron paramagnetic resonance of a copper doped $[(CH_3)_2NH_2][Zn(HCOO)_3]$ hybrid perovskite framework, *Phys. Chem. Chem. Phys*. **2018**, *20*, 12097–12105.

(27) Šimėnas, M.; Klose, D.; Ptak, M.; Aidas, K.; Mączka, M.; Banys, J.; Pöppl, A.; Jeschke, G. Magnetic excitation and readout of methyl group tunnel coherence, *Sci. Adv*. **2020**, *6*, eaba1517.

(28) Orio, M.; Bindra, J. K.; Tol, J. v.; Giorgi, M.; Dalal, N. S.; Bertaina, S. Quantum dynamics of Mn^{2+} in dimethylammonium magnesium formate, *J. Chem. Phys*. **2021**, *154*, 154201.

(29) Usevičius, G.; Eggeling, A.; Pocius, I.; Kalendra, V.; Klose, D.; Mączka, M.; Pöppl, A.; Banys, J.; Jeschke, G.; Šimėnas, M. Probing methyl group tunneling in $[(CH_3)_2NH_2][Zn(HCOO)_3]$ hybrid perovskite using Co^{2+} EPR, *Molecules* **2023**, *28*, 979.

(30) Weng, D.-F.; Wang, Z.-M.; Gao, S. Framework-structured weak ferromagnets, *Chem. Soc. Rev*. **2011**, *40*, 3157–3181.

(31) Ptak, M.; Sieradzki, A.; Šimėnas, M.; Maczka, M. Molecular spectroscopy of hybrid organic–inorganic perovskites and related compounds, *Coord. Chem. Rev.* **2021**, *448*, 214180.

(32) García-Ben, J.; McHugh, L. N.; Bennett, T. D.; Bermúdez-García, J. M. *Coord. Chem. Rev.* **2022**, *454*, 214337.

(33) Boča, R. Rajnák, C.; Titiš, J.; Valigura, D. Field supported slow magnetic relaxation in a mononuclear Cu(II) complex, *Inorg. Chem*. **2017**, *56*, 1478–1482.

(34) Cui, H.-H.; Lv, W.; Tong, W.; Chen, X.-T.; Xue, Z.-L. Slow magnetic relaxation in a mononuclear five-coordinate Cu(II) complex, *Eur. J. Inorg. Chem*. **2019**, *2019*, 4653–4659.

(35) Wakizaka, M.; Arczynski, M.; Gupta, S.; Takaishi, S.; Yamashita, M. Spin dynamics in a heisenberg weak antiferromagnetic chain of an iodide-bridged Cu(II) complex, *Dalton Trans.*, DOI: 10.1039/D3DT01840G.

(36) Wakizaka, M.; Ishikawa, R.; Tanaka, H.; Gupta, S.; Takaishi, S.; Yamashita, M. Creation of a field-induced Co(II) single-ion magnet by doping into a Zn(II) diamagnetic metal–organic framework, *Small* **2023**, 2301966.

(37) Hu, K.-L.; Kurmoo, M.; Wang, Z.; Gao, S. Metal–organic perovskites: synthesis, structures, and magnetic properties of $[C(NH_2)_3][M^{II}(HCOO)_3]$ (M=Mn, Fe, Co, Ni, Cu, and Zn; $C(NH_2)_3$= Guanidinium), *Chem. Eur. J.* **2009**, *15*, 12050–12064.

(38) Neese, F.; Wennmohs, F.; Becker, U.; Riplinger, C. The ORCA quantum chemistry program package, *J. Chem. Phys*. **2020**, *152*, 224108.

(39) Chilton, N. F.; Anderson, R. P.; Turner, L. D.; Soncini, A.; Murray K. S. PHI: a powerful new program for the analysis of anisotropic monomeric and exchange-coupled polynuclear d- and f-block complexes, *J. Comput. Chem*. **2013**, *34*, 1164–1175.

(40) Topping, C. V.; Blundell, S. J. A.C. susceptibility as a probe of low-frequency magnetic dynamics, *J. Phys.: Condens. Matter* **2019**, *31*, 013001.

(41) Stoll, S.; Schweiger, A. EasySpin, a comprehensive software package for spectral simulation and analysis in EPR, *J. Magn. Reson.* **2006**, *178*, 42–55.

(42) Epel, B.; Gromov, I.; Stoll, S.; Schweiger, A.; Goldfarb, D. Spectrometer manager: a versatile control software for pulse EPR spectrometers. *Concepts Magn. Reson. Part B* **2005**, *26B*, 36–45.

Table of Contents

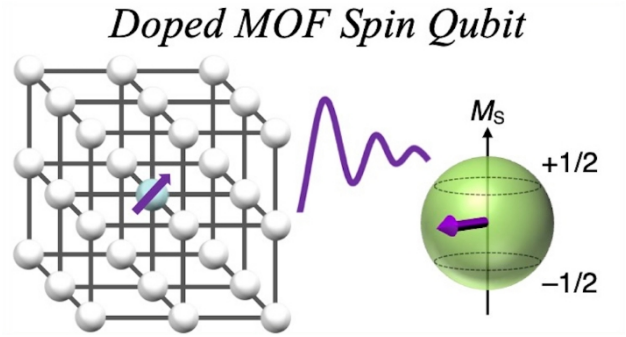

Figures

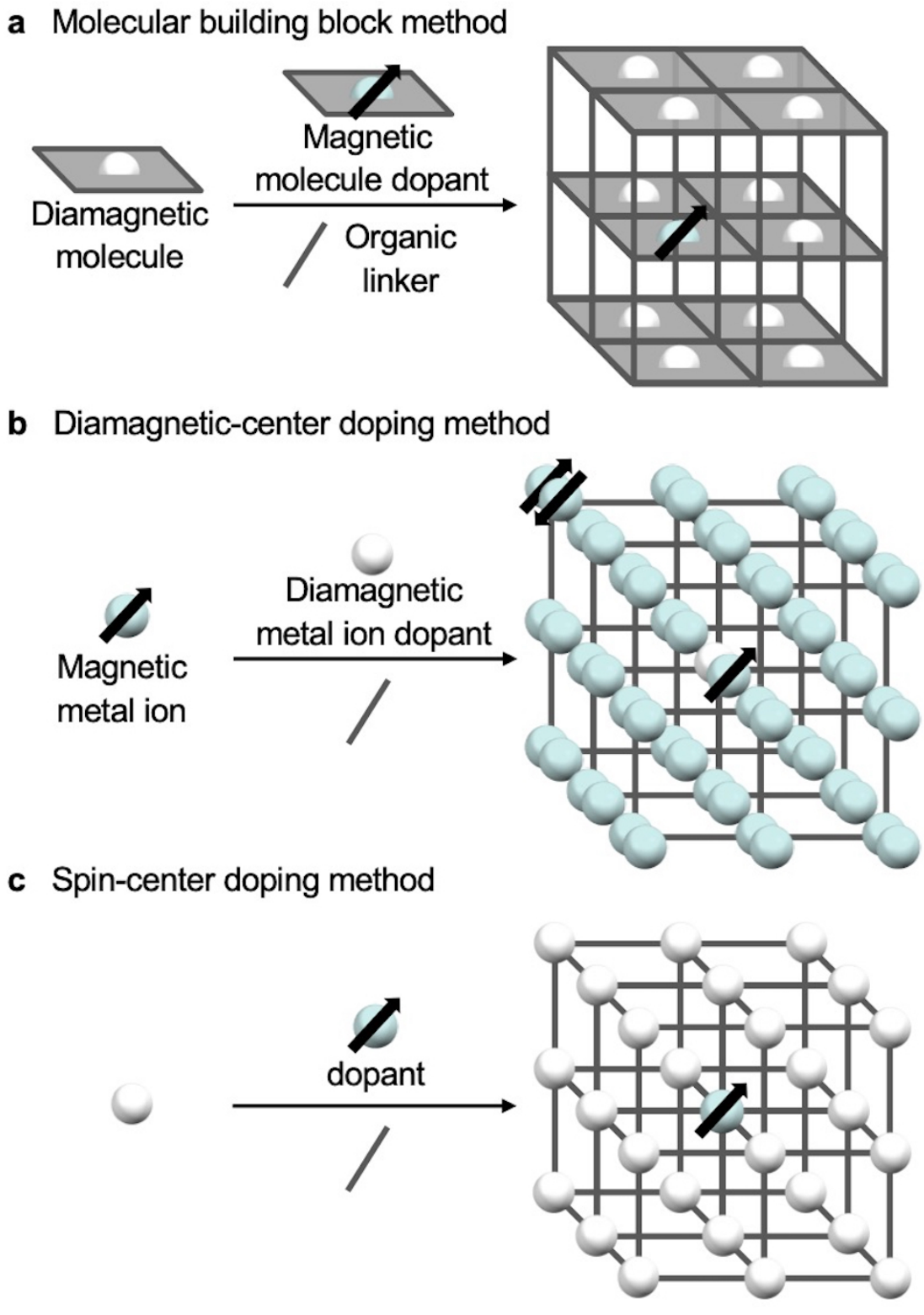

Figure 1

Schematic of the general methods to prepare MOF-based spin qubits, e.g., $[V^{IV}_{x}Ti^{IV}_{1-x}O(TCPP\text{-}Zn_2\text{-}bpy)]$ (TCPP = tetracarboxylphenylporphyrinate; bpy = 4,4'-bipyridyl),[20] $[Zn_{0.03}Cu_{2.97}(tricarboxylate)_2]$,[21] and

$[CH_3(NH_2)_2][Mn^{II}_xZn^{II}_{1-x}(HCOO)_3]$:[25] (a) molecular building block method, (b) diamagnetic-center doping method, and (c) spin-doping method.

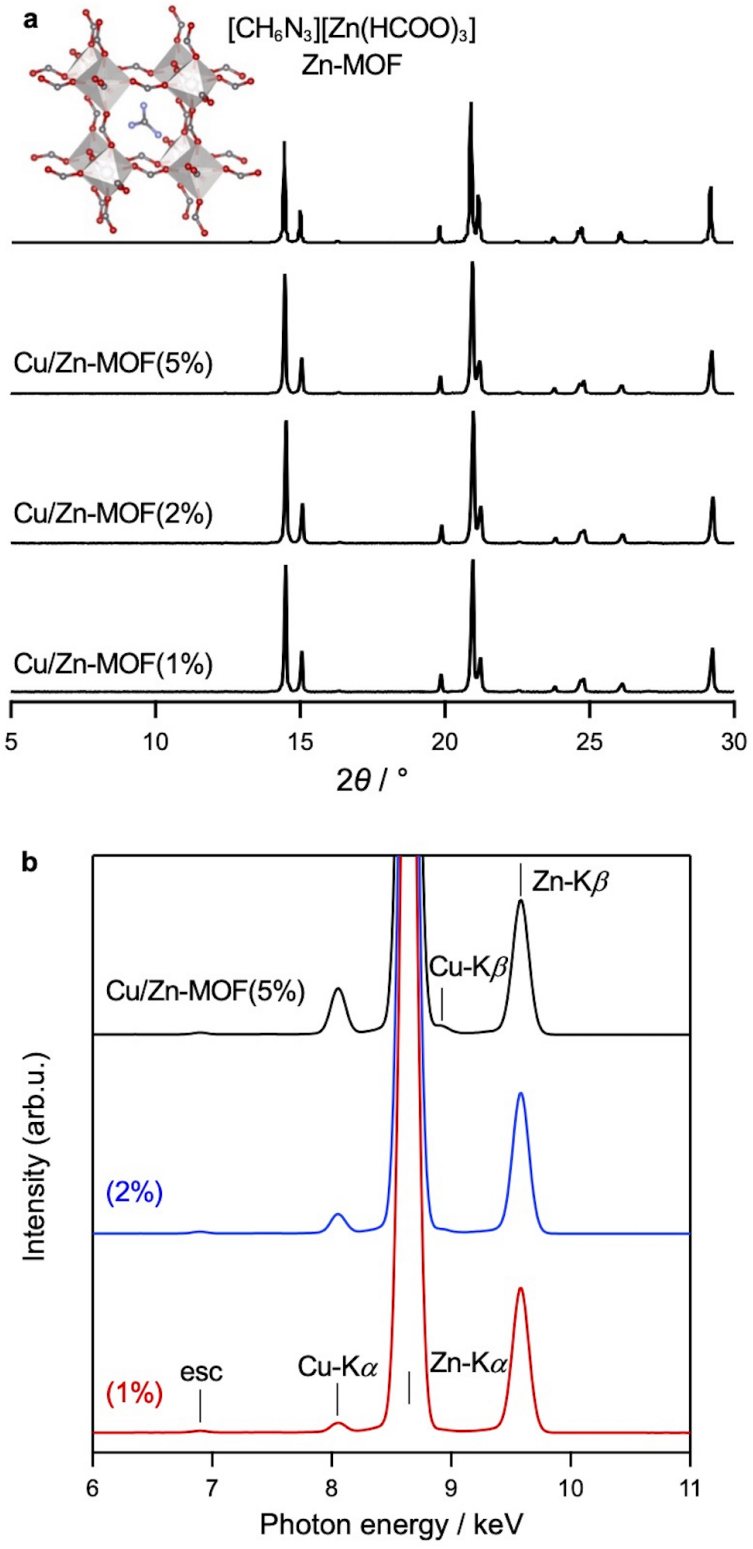

Figure 2

(a) PXRD patterns and (b) XRF spectra of Cu/Zn-MOF(5%), Cu/Zn-MOF(2%), and Cu/Zn-MOF(1%) and the crystal structure and PXRD pattern of $[CH_6N_3][Zn(HCOO)_3]$ (Zn-MOF).[37] The escape (esc) peak stems

from Cu-Kα.

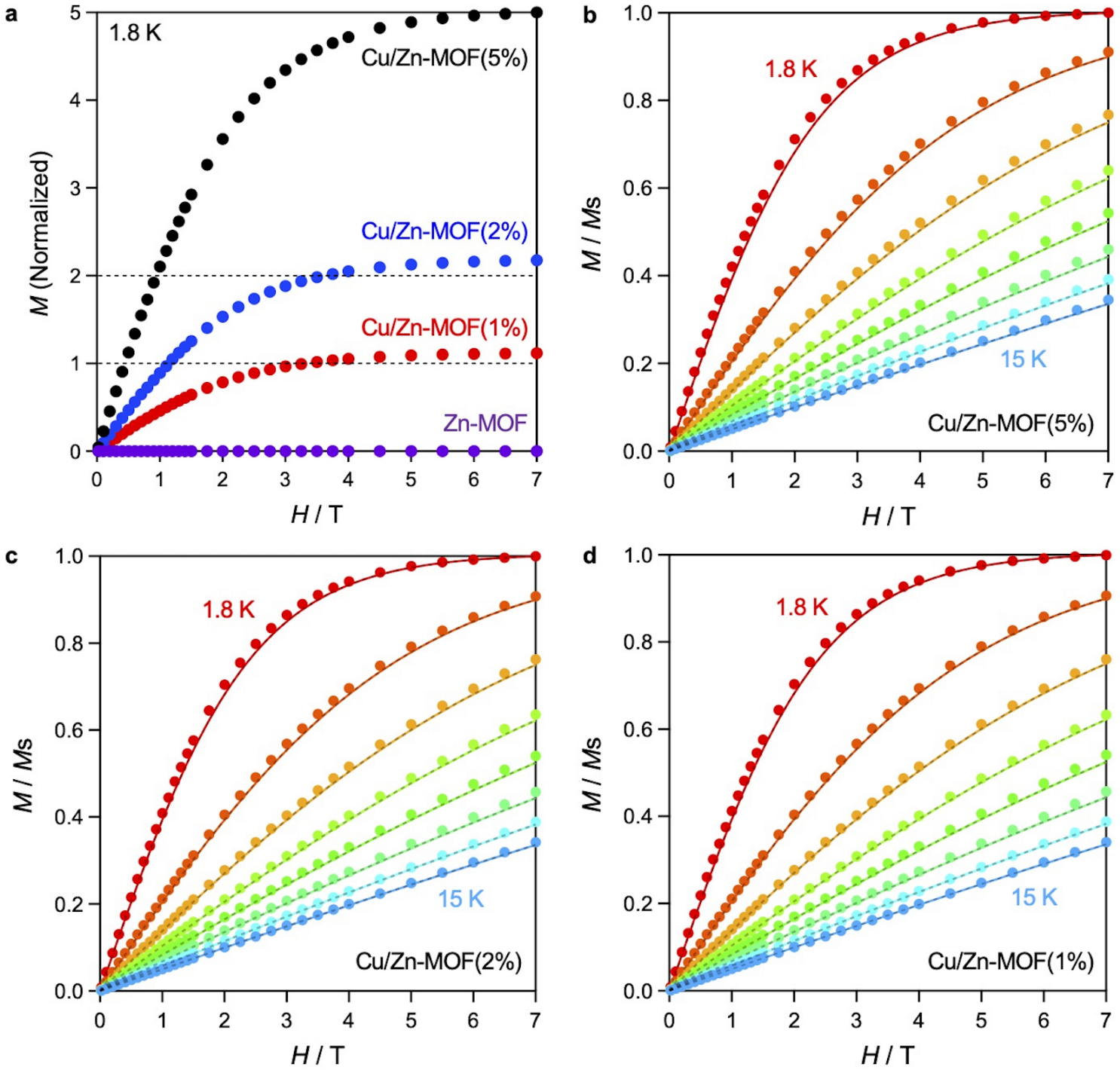

Figure 3

Magnetization–field (M–H) curves normalized by the saturation M (M_S) at 1.8 K of (a, b) Cu/Zn-MOF(5%), (c) Cu/Zn-MOF(2%), and (d) Cu/Zn-MOF(1%). The temperature dependency was measured at 1.8, 3.6, 5.4, 7.2, 9.0, 11, 13, and 15 K. The solid colored curves and the dotted gray curves (they are overlapping) represent the normalized simulation curves using the values obtained from CASSCF, i.e., g_x = 2.09, g_y = 2.12, g_z = 2.52, and ESR, i.e., g_x = 2.065, g_y = 2.120, and g_z = 2.435, respectively.

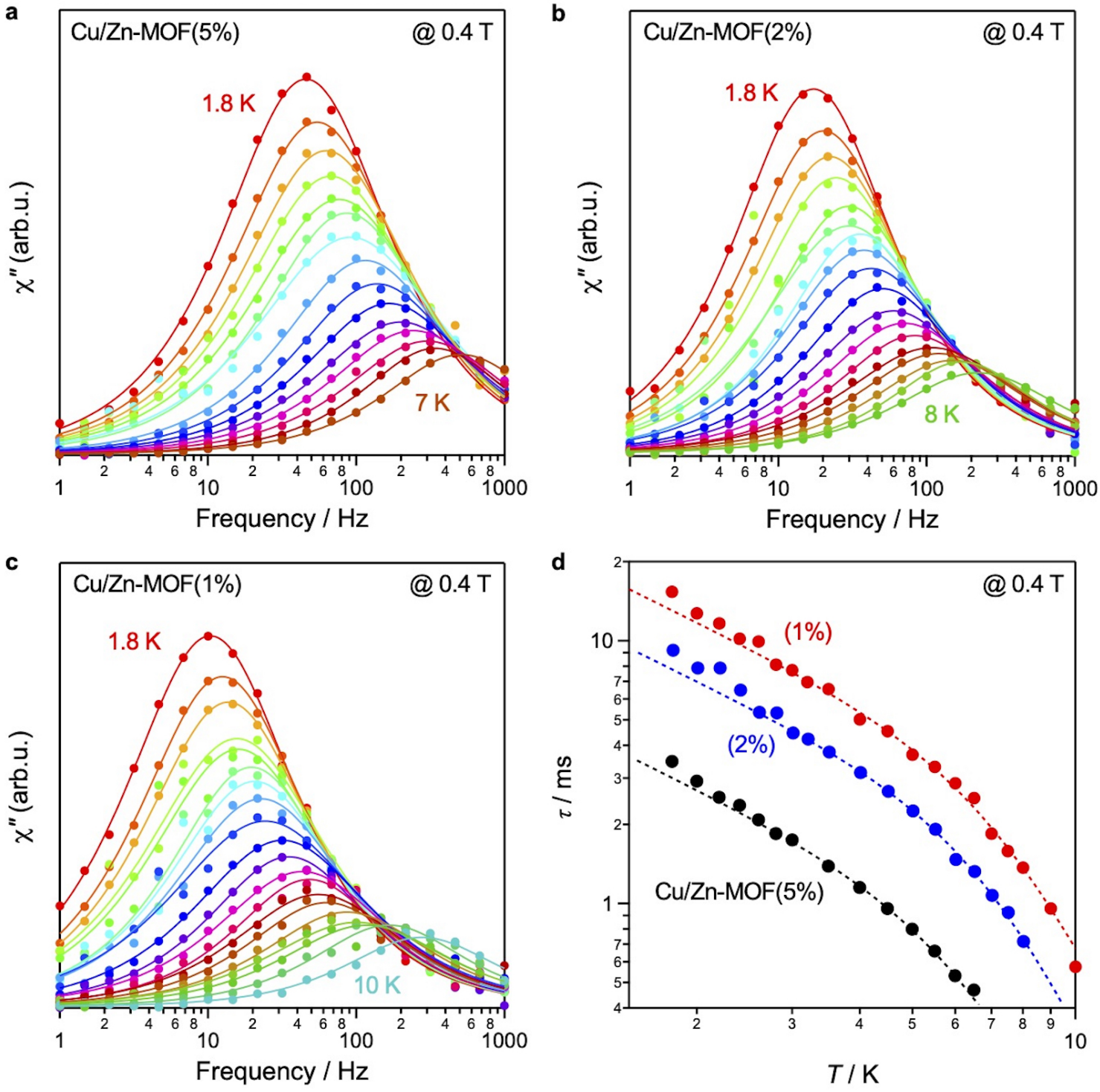

Figure 4

Imaginary part of the AC susceptibility (χ'') of (a) Cu/Zn-MOF(5%), (b) Cu/Zn-MOF(2%), and (c) Cu/Zn-MOF(1%) measured at 1.8–7.0, 1.8–8.0, and 1.8–10 K over a range of 1–1000 Hz under a static magnetic field of 0.4 T, respectively. Each line is a Debye-relaxation-fitting curve. (d) Log-scale plots of magnetic relaxation time (t) versus temperature (T) for Cu/Zn-MOF(5%), Cu/Zn-MOF(2%), and Cu/Zn-MOF(1%) measured under a static magnetic field of 0.4 T. The dotted lines represent the fitting curves obtained using the direct and Raman processes.

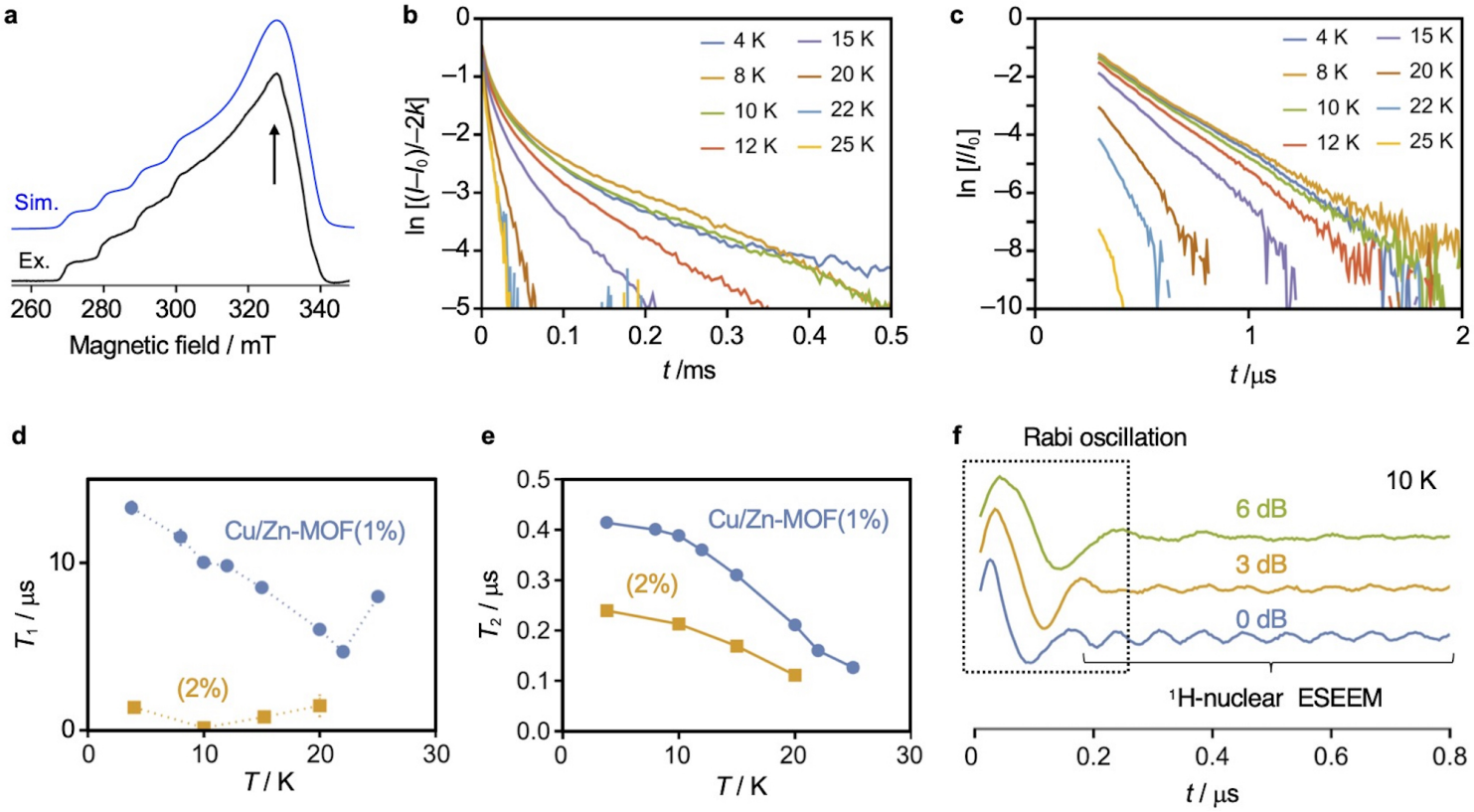

Figure 5

X-band pulse ESR measurements. (a) Hahn-echo-detected ESR spectrum of Cu/Zn-MOF(1%) at 3.8 K under microwave irradiation of 9.689126 GHz, together with that of a simulation applied g_x = 2.065(20), g_y = 2.120(60), g_z = 2.435(20), $^{Cu}A_x = {}^{Cu}A_y$ = 60 MHz, $^{Cu}A_z$ = 330 MHz, and lwpp = Gaussian (0.6 mT) + Lorentzian (0.6 mT) using EasySpin.[41] (b) Inversion recovery time (T_1) and (c) Hahn echo decay time (T_2) of Cu/Zn-MOF(1%) at 4, 8, 10, 12, 15, 20, 22, and 25 K under a magnetic field of 328 mT. Temperature dependency of (d) T_1 and (e) T_2 of Cu/Zn-MOF(1%) and Cu/Zn-MOF(2%). (f) Rabi oscillation of Cu/Zn-MOF(1%) at 10 K for different microwave powers (0, 3, and 6 dB). The fine oscillation at a later time region is due to ^{1}H electron spin echo envelope modulation (ESEEM).

Supplementary Files

This is a list of supplementary files associated with this preprint. Click to download.

- Supportinginformation.pdf
- TableOfContent.jpg